Reversal of the chiral anomaly bulk states with periodically staggered potential

Han-Rong Xia [1] and Meng Xiao [1,2,*]

[1] *Key Laboratory of Artificial Micro- and Nano-Structures of Ministry of Education and School of Physics and Technology, Wuhan University, Wuhan 430072, China*

[2] *Wuhan Institute of Quantum Technology, Wuhan 430206, China*

(Received 27 November 2022; revised 5 January 2023; accepted 12 January 2023; published 25 January 2023)

A chiral anomaly Landau level emerges when a Weyl semimetal is subjected to an external magnetic field. Recently, it was demonstrated that similar chiral anomaly bulk states exist within two-dimensional Dirac semimetals if proper boundary conditions are applied. The resulting chiral bulk states disperse linearly with the slope determined by a combination of the boundary condition and chirality of the Dirac cone, i.e., whether it is at K or K' point. In this paper, we show that the slope (the sign of group velocity) near the K and K' points can be reversed under a periodically staggered potential. We first analyze the parameter dependence of this phenomenon with a nearest-neighbor tight-binding model. Then, we give a semianalytical solution for the dispersion of the chiral anomaly bulk states. In the end, we provide a photonic crystal system and prove with full-wave simulations that such a phenomenon can indeed be observed.

DOI: 10.1103/PhysRevB.107.035144

I. INTRODUCTION

Topological semimetals have attracted intense attention in the last decades [1–17]. Three-dimensional (3D) Weyl semimetals, as a representative type of topological semimetals, exhibit band degeneracies protected by discretized Chern numbers [7–17]. These topological band degeneracies, i.e., topological charges, can only be annihilated by another topological band degeneracy with an opposite topological charge. Besides the associated Fermi arcs [7,8,12], the response of Weyl semimetals when subjected to an external magnetic field (or an artificial gauge field) also draws a great deal of research interests [10,18–22]. The applied B field quantizes the system spectra to discretized Landau levels. Different from two-dimensional (2D) Dirac semimetals where the Landau levels are all flat [23–25], the zeroth-order Landau level at a Weyl point disperses linearly in the direction determined by the charge of the Weyl point and the direction of the applied B field. Such a peculiar chiral Landau level consists of unidirectional bulk states [dubbed as chiral anomaly bulk states (CABSs)], and is of fundamental importance as it contributes to the chiral anomaly effect and negative magnetoresistance [10].

Enabled by the flexibility in sample fabrication and experimental measurement, classical wave systems such as photonic crystals (PCs) and phononic crystals offer ideal platforms for studying new physics and exotic phenomena related to topological phases [26–28]. For example, the gauge fields in classical wave systems can be generated by dynamic modulation or locally varying the structure parameters [11,29–34]. Experiments have demonstrated the presence of the gauge field and quantized Landau levels induced by local deformation of the graphene lattice in both photonics and acoustics [30–32]. Later on, the CABSs due to the gauge field introduced by local deformation have also been observed in 3D photonic and acoustic Weyl semimetals as well as in a 2D photonic Dirac semimetal [33,35,36]. Very recently, Wang *et al.* showed that CABSs can be generated by simply imposing a specific boundary condition on a 2D Dirac semimetal [37]. Different from all previous cases, herein the CABSs do not require the presence of external magnetic fields or synthetic gauge fields introduced by local structural variations. The CABSs are locally unidirectional and provide robust transport that is phenomenally the same as valley transport [38,39]. The only difference compared with valley transport is that the transport here is inside the bulk, not localized on the boundary or domain wall.

The unidirectional transport of the CABSs is ensured by the positive- (negative-) definite group velocity of the corresponding band dispersion. Here we show that the sign of group velocity can change locally with a periodically staggered potential. By changing the periodicity or potential depth, the group velocity of the CABSs can change gradually from positive to zero and then negative (or the other way around). We first demonstrate this phenomenon numerically with a tight-binding model. Then, we show that this behavior can be captured with a 2D Dirac Hamiltonian under a staggered potential. With this, we provide a semianalytical formula for the dispersion of the CABSs. Here, the dependence on the periodicity and potential depth is included, however not given explicitly. One can numerically solve the formula and see how the dispersion changes with the periodicity and potential depth (that is why we call it semianalytical). After that, we show with full-wave simulations that the aforementioned phenomena can be observed with a photonic crystal inside a coaxial waveguide. The ability to change the propagation direction of the CABSs offers

*phmxiao@whu.edu.cn

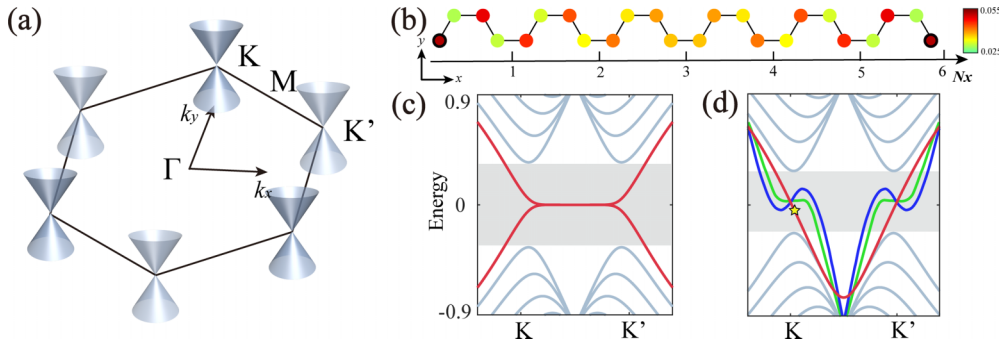

FIG. 1. Dirac cone and possible CABS for a finite system. (a) First Brillouin zone of a graphene lattice with conical dispersion at the K and K' points. (b) A strip of graphene lattice which is finite along the x direction and periodic along the y direction. The number of unit cells along the x direction is N_x. Color code denotes the field-intensity distribution of one typical CABS [marked by the yellow star in (d)]. (c), (d) Band dispersion of the graphene lattice in (b), where the onsite potential of the outmost atoms (marked by the bold black circles) is kept at zero in (c) and set as $U = -0.75$ in (d). Red lines in (c) highlight the edge states while the red lines in (d) denote the CABSs. Green and blue lines sketch the evolution of CABSs for later purpose. Except for the green and blue lines in (d), all the other lines are calculated within a nearest-neighbor tight-binding model in which the hopping constant is set as 1. The number of unit cells is fixed at $N_x = 6$ in (c) and (d).

new freedom in wave transports. Meanwhile, in contrast to edge states, there the bulk states use almost all the available guiding space which can benefit a wide variety of topological applications such as topological lasers and robust information transportation [40–45].

The paper is organized as follows. In Sec. II, we introduce the basic concepts about the CABSs. In Sec. III, we give a tight-binding model that the group velocity of CABSs can be altered with either the potential depth or periodicity. In Sec. IV, we provide the semianalytical solution for the dispersion of the CABSs. In Sec. V, we offer a possible PC for observing these phenomena and demonstrate them with full-wave simulations. Finally, we summarize in Sec. VI.

II. CABS IN A FINITE SYSTEM

It is well known that a honeycomb lattice such as graphene exhibits 2D Dirac cone dispersion in the reciprocal space at the K and K' points. Figure 1(a) shows the first Brillouin zone of the periodic graphene lattice and the sketch of Dirac cones. The Dirac cone degeneracy here is protected by the combination of time-reversal symmetry and inversion symmetry. A global potential gating only shifts the energy of the Dirac cones and cannot lift the degeneracy. If we consider a strip of graphene lattice which is finite along the x direction and periodic along the y direction as shown in Fig. 1(b), there will be a "pseudogap" induced by the finite width in the x direction [shaded region in Figs. 1(c) and 1(d)]. Here, we consider the nearest-neighbor tight-binding model and the hopping constant is set as 1. The dispersions of the bulk states become quadratic near the K and K' points as shown with gray lines in Figs. 1(c) and 1(d). Meanwhile, if no decoration is added on the boundary, there will be two nearly flat edge states connecting band dispersion between the K and K' points [see red lines in Fig. 1(c)]. These two edge states originate from the hybridization of the edge states on the zigzag boundary of a graphene lattice [46]. As we gradually increase the potential of the outermost column of atoms [47], the dispersion of the edge state will be deformed and merged into the bulk gradually, as shown with the red line in Fig. 1(d). Similar dispersions were observed in acoustic systems where one changed the truncation position of the boundary so as to effectively change the potential of the boundary layer [37]. Note here even though the red line in Fig. 1(d) penetrates through the pseudogap, it is still a bulk state. This fact can be seen with the color code in Fig. 1(b) for the field distribution of a typical state (marked by the yellow star). Thus, the red line represents bulk modes with chiral anomaly inside a pseudogap [37]. The sign of group velocity, i.e., slope of dispersion, is determined by the chirality of the Dirac cone (which is opposite for the K and K' valley) and the sign of added potential on the outermost column (or truncation position of the boundary for PC and acoustic systems). See more detailed discussion in the Appendix A. In the following, we will show that the slope of dispersion at the K point can be gradually tuned from positive to zero and then reversed (or the other way around), as sketched with the green (flat) and blue (reversed) lines in Fig. 1(d).

III. REVERSAL OF THE CABS

To achieve the aforementioned evolution, we put the graphene lattice inside a periodically staggered potential as shown in Fig. 2(a). Here, the onsite potential of the left- (right) half is set as $-U$ $(+U)$ as denoted by the shadow cyan (red) background. The number of total graphene lattices along the x direction is set as $2N_x$ with N_x for each half. The supercell is periodic in the x direction and infinite along the y direction. Note here, we only change the potential between different unit cells, and the potential of the two sublattices in the same unit cell are still the same. The outermost atoms in each half are exposed to a potential jump of $\pm 2U$ at the two boundaries. Hence, as discussed in Fig. 1(d), two CABSs with opposite group velocities at the projection of both the K and K' points would be expected. This feature is shown in Fig. 2(b), where the gray lines represent bulk bands, and the red and blue lines

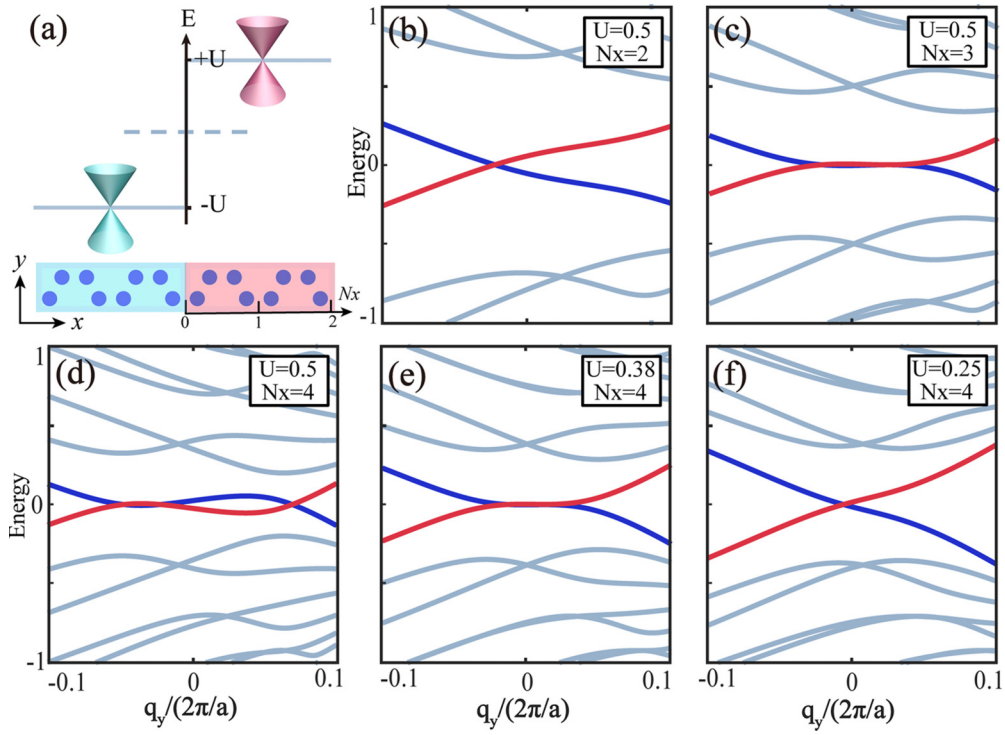

FIG. 2. Evolution of CABSs under periodically staggered potential. (a) Sketch of the tight-binding model. Onsite potential is $-U$ for the left half and $+U$ for the right half. The lattice is infinite in the y direction and periodic horizontally with a total unit number $2N_x$. (b)–(f) Band dispersions for different combinations of U and N_x, where the CABSs are highlighted in red and blue. Only the nearest-neighbor hopping is considered here with the hopping constant set as 1. q_y is the wave vector relative to the K point in the y direction.

for the CABSs with positive and negative group velocities at the K points, respectively. Here, q_y represents the wave vector away from the projection of the K point along the y direction. The band dispersions at the K' point can be obtained by reversing the direction of q_y since the band dispersions at the K and K' points are related by the inversion symmetry. Note here the crossing of the red and blue lines is at zero energy but not necessarily at $q_y = 0$.

Now we proceed to see the evolution of these CABSs under the change of staggered potential depth U and periodicity N_x. Figures 2(b)–2(f) show the corresponding band dispersions with different combinations of U and N_x. First, we fix $U = 0.5$ and change N_x. As shown in Figs. 2(b)–2(d), with the increase of N_x, the slopes of CABSs first become flat [Fig. 2(c)] around the K point and then reverse sign if we further increase N_x [Fig. 2(d)]. Similar features are also observed in Figs. 2(e) and 2(f) where we fix $N_x = 4$ and tune U. At $U = 0.38$, the slopes of CABSs are flat and at $U = 0.25$ the signs of slopes become the same as Fig. 2(b). As the lattice number N_x further increases, the band dispersions of these CABSs become winding together with more and more degeneracy points between the red band and blue band.

IV. SEMIANALYTICAL SOLUTIONS

To understand the evolution of these CABSs, we give a semianalytical solution for their dispersions. The behavior of the tight-binding model can be captured with the gated 2D Dirac Hamiltonian:

$$\mathrm{H} = v_F(q_x\sigma_x \pm q_y\sigma_y) + V(x), \tag{1}$$

where v_F is the Fermi velocity at the Dirac point (when the nearest hopping and lattice constants are set as 1, $v_F = \sqrt{3}\hbar/2$), $\sigma_{x,y,z}$ are Pauli matrices, q_x and q_y are wave vectors relative to the K (+ sign in the bracket) or K' (− sign in the bracket) in the x- and y directions, respectively. The staggered potential V is

$$V(x) = \begin{cases} V_L = -U, & -L \leqslant x < 0, \\ V_R = U, & 0 \leqslant x \leqslant L, \end{cases} \tag{2}$$

where $2L$ is the width of the system in the x direction. Here, q_y is conserved, and we remove $e^{iq_y y}$ in the wave function for simplicity. The wave functions inside the left- and right halves are

$$\psi_{L,R}(x) = A_{L,R}\begin{pmatrix} 1 \\ s_{L,R}e^{i\phi_{L,R}} \end{pmatrix} e^{iq_{Lx,Rx}x} + B_{L,R}\begin{pmatrix} 1 \\ s_{L,R}e^{i(\pi-\phi_{L,R})} \end{pmatrix} e^{-iq_{Lx,Rx}x}, \tag{3}$$

where $q_{Lx,\,Rx} = \sqrt{(V_{L,R}-E)^2/v_F^2 - q_y^2}$, $\phi_{L,R} = \arctan(q_y/q_{Lx,Rx})$, $s_{L,R} = \mathrm{sgn}(E - V_{L,R})$. Here, the first term and second term represent the right- and left-propagating waves, respectively. The coefficients $A_{L,R}$ and $B_{L,R}$ are determined self-consistently with the continuity of the wave functions at

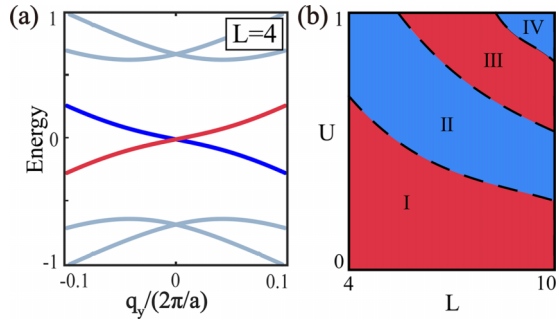

FIG. 3. Semianalytical solutions. (a) Band dispersion calculated with the semianalytical solution in Eq. (5), where gray lines represent the bulk bands, while the red and blue lines denote the CABSs. (b) Sign of Δ defined in Eq. (6) as a function of L and U. Red regions represent $\Delta > 0$, blue for $\Delta < 0$, and black dashed lines denote the transitions whereat $\Delta = 0$. $L = 4$ and $U = 0.5$ in (a), and $v_F = \sqrt{3}/2$ for (a), (b).

the boundary,

$$\psi_L(0) = \psi_R(0), \quad \psi_L(-L) = \psi_R(L). \tag{4}$$

Solving these equations, we arrive at the semianalytical expression for the mode dispersion.

$$[-1 + \cos(q_{Lx}L)\cos(q_{Rx}L)]\cos\phi_L + \sin(q_{Lx}L)\sin(q_{Rx}L)(\sec\phi_R + \sin\phi_L\tan\phi_R) = 0. \tag{5}$$

Figure 3(a) shows the dispersion at $L = 4$, $U = 0.5$ in the vicinity of the K point. Same as before, the gray lines are bulk modes, and the red and blue lines for the dispersion of the CABSs. Note that the band structures from the effective Hamiltonian exhibit some differences from the tight-binding model because the Dirac Hamiltonian can only well describe the conelike dispersion near the Dirac point. We use the group-velocity difference between the red and blue lines at their crossing point to characterize the sign change of the slope,

$$\Delta = \frac{\partial E_r}{\partial q_y} - \frac{\partial E_b}{\partial q_y}\bigg|_{E_r = E_b}, \tag{6}$$

where E_r and E_b represent the energy of the red and blue lines, respectively. When there are multiple crossing points where $E_r = E_b$ [say, Fig. 2(d)], we choose the central crossing point. Thus, for the normal case as shown in Figs. 2(b) and 2(f) and Fig. 3(a), $\Delta > 0$. $\Delta = 0$ when the CABSs are flat [say, Figs. 2(c) and 2(e)] while $\Delta < 0$ when the slope is reversed [Fig. 2(d)]. Figure 3(b) plots the sign of Δ as a function of U and L. The red regions represent $\Delta > 0$, blue for $\Delta < 0$, and the black dashed lines for critical values at which $\Delta = 0$. We can see that as L increases, the threshold potential of each sign reversal decreases; thus, more and more windings appear in the band diagram.

V. PHOTONIC REALIZATIONS

The Dirac cone dispersion presented in Fig. 1(a) can be easily realized in a 2D honeycomb PC. To introduce the potential difference, we consider two different unit cells with slightly changed radius as shown in Fig. 4(a), where the radii of the dashed circles are the same, which are plotted here as a reference. Here, the solid disks represent dielectric cylinders with relative permittivity $\varepsilon_r = 16$ and the background is air. The lattice constant is set as $a = 8$ mm. Figure 4(b) shows the corresponding band structure when the electric field points out of plane, with $r_1 = 1.2$ mm and $r_2 = 1.3$ mm. The band dispersion for $r_1 = 1.2$ mm (magenta lines) is shifted slightly upward relative to that for $r_2 = 1.3$ mm (cyan lines) as illustrated in Fig. 4(b). Meanwhile, the group velocity at the Dirac cone is also slightly changed, which however does not change the feature we intend to see. In practice, such 2D PCs are realized by sandwiching cylinders of finite height with perfect electric conductor (PEC) boundary, i.e., dielectric cylinders inside PEC waveguides. When the height of cylinders H is small, only the modes with the polarization of the electric field perpendicular to the PEC boundary are allowed for the lower-frequency range. Here, we set $H = 5$ mm and get a clean Dirac cone band dispersion inside the frequency range of interest from 8 to 12 GHz.

We then further wrap the PEC waveguide onto a concentric cylinder as shown in Fig. 4(c) to achieve the periodic boundary condition. Here, for illustration, the top layer of PEC is set as transparent. Since there is no other mode around this frequency range, this wrapping process only slightly deforms the band dispersion. The band diagrams for $r_1 = r_2$ are exhibited in the Appendix B for comparison. Details about the simulations are provided in the Appendix C. Figures 4(d)–4(f) show the band dispersions calculated with a full-wave simulation software, COMSOL MULTIPHYSICS™, when N_x are 4, 5, and 8, respectively. Same as before, the bands of CABSs are highlighted in red and blue. The numerical simulations confirm the band dispersion as discussed before, i.e., with the increase of N_x, the slope of CABSs first becomes flat and then reverses. This evolution can also be done with the increase of U, which is investigated in the Appendix D.

VI. SUMMARY

In summary, we investigate the intriguing band-dispersion evolution of the CABSs in the honeycomb lattice under periodically staggered potential. We show that the group velocity of the CABSs can be positive, zero, and negative near the K point depending on the number of lattices along the x direction and depth of the staggered potential. We give a semianalytical solution for the dispersions of the CABSs. After that, we also propose a PC system to simulate the phenomena discussed above. In our approach, the parameters can be flexibly tuned and the group velocity of the CABSs can be easily adjusted accordingly. Our work offers freedom in controlling the propagation of CABSs, and points to promising applications. First, the control of the group velocity can be used in regulating information transmission and beam splitting [48]. Second, the bulk property of these CABSs can benefit the larger area and higher-throughput transmission, for example, bulk topological transport in topological laser [40]. Finally, the flat-band dispersion is also fairly promising and can lead to potential applications related to slow light [49].

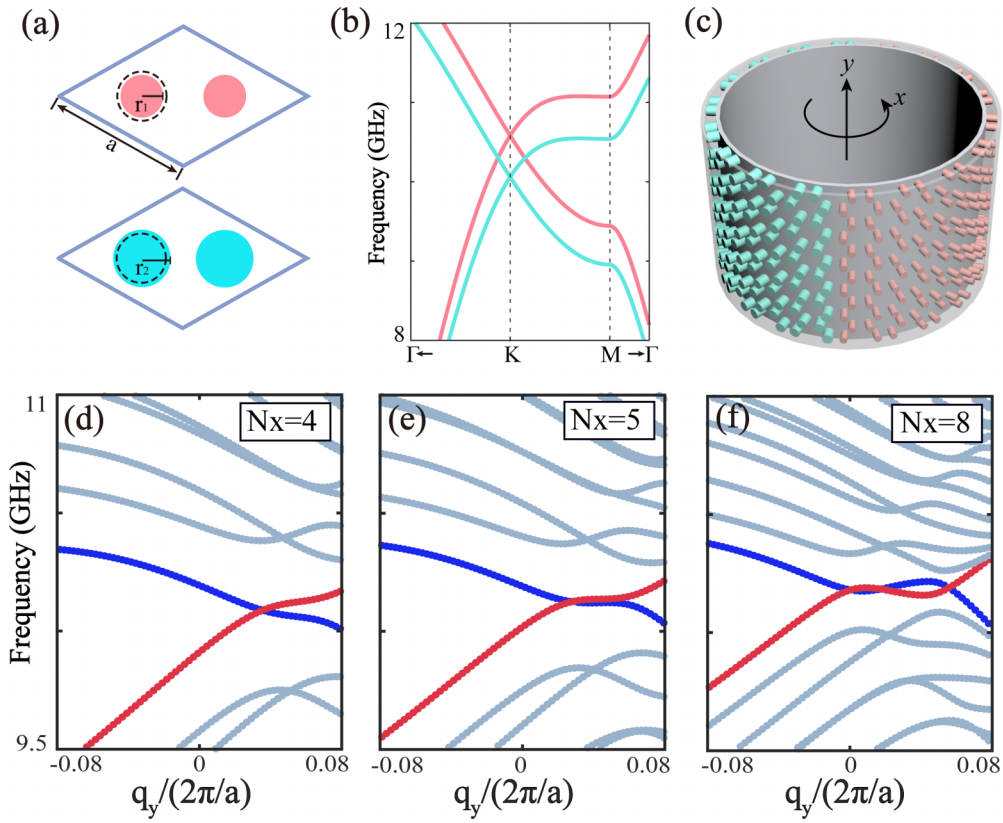

FIG. 4. Realizations with PCs. (a) Unit cells of two 2D honeycomb lattices. Solid disks represent dielectric cylinders, where the radii of cylinders for the upper- and lower unit cells are slightly different. Here, black dashed circles share the same radius. (b) Band structure for the unit cells in (a), where $r_1 = 1.2$ mm, $r_2 = 1.3$ mm, and $a = 8$ mm; relative permittivity of the dielectric cylinder is $\varepsilon_r = 16$ and background is air with relative permittivity 1. (c) Dielectric cylinders with finite height $H = 5$ mm in honeycomb lattice are sandwiched by two PEC boundaries, and are then wrapped on a larger concentric cylindrical waveguide. Here, the outer PEC boundary is set as transparent for illustration. (d)–(f) Band structures of the system in (c) for different N_x, where the average lattice constant is kept at $a = 8$ mm. All other parameters are the same as (b).

ACKNOWLEDGMENTS

This work is supported by the National Natural Science Foundation of China (Grant No. 12274332) and the National Key Research and Development Program of China (Grant No. 2022YFA1404901). M.X. is also supported by the startup funding of Wuhan University.

APPENDIX A

See Fig. 5. When we reverse the onsite potential of the outermost atoms, the slope of the CABSs is reversed accordingly.

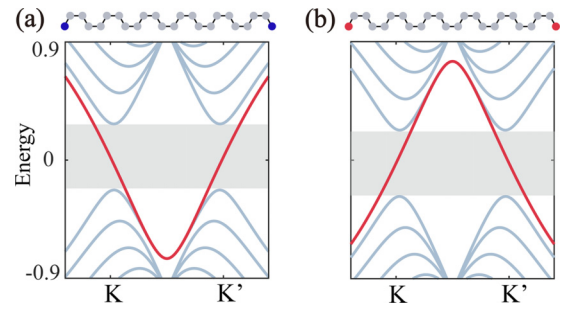

FIG. 5. Dispersion of CABSs for different boundary decorations. Onsite potential of the outermost column is set as U, with $U = -0.75$ in (a) and $U = 0.75$ in (b). Here, gray lines represent bulk bands while red lines denote the dispersion of the CABSs.

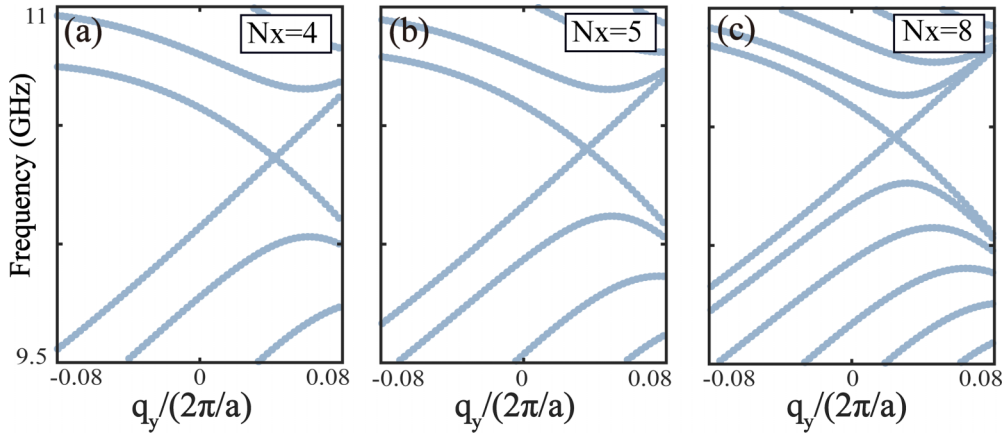

FIG. 6. Band diagram for $r_1 = r_2 = 1.2$ mm with different N_x. Other parameters are the same as those in Fig. 4.

APPENDIX B

The band structures for different N_x when $r_1 = r_2 = 1.2$ mm are shown in Fig. 6. The linear dispersion is seen near 10.4 GHz.

APPENDIX C

We design a wrapped PC as illustrated in Fig. 4(c) and use the commercial software COMSOL for full-wave simulations. The RF module is used to find the eigenfrequency. The supercell is shown in Fig. 7. Here, the top surface as well as the bottom are set as periodic boundaries. The outer- and inner-cylindrical surfaces are set as PEC boundaries. The relative permittivity of the dielectric cylinders we use is $\varepsilon_r = 16$, which can be realized with ceramic dielectric materials in microwave region.

APPENDIX D

The dependence of CABSs on U is shown in Fig. 8. Here we fix $N_x = 4$ and increase r_2 to effectively increase the potential depth U. As expected, the sign change of slope is observed.

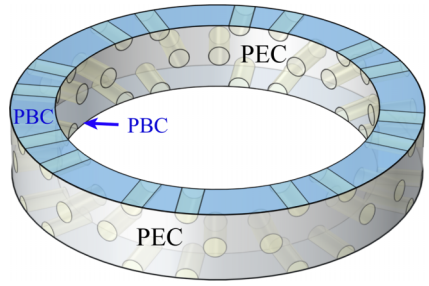

FIG. 7. Geometry of the supercell for $N_x = 4$ and $r_1 = r_2$. Top and bottom surfaces (colored blue) are set as periodic boundary conditions (PBC). The outer- and inner-cylindrical surfaces (in gray color) are set as PEC boundaries. Yellow cylinders inside represent dielectric pillars.

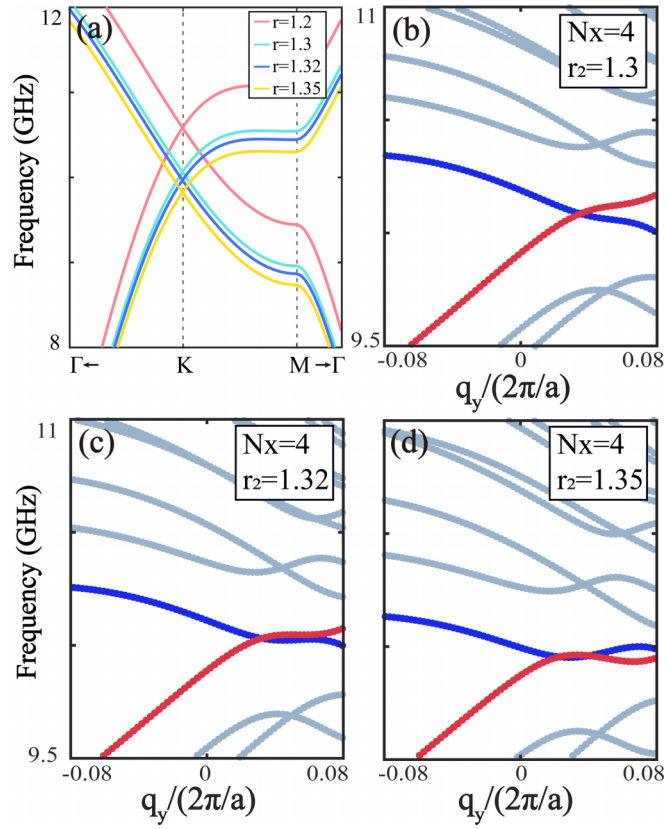

FIG. 8. Evolution of CABSs when increasing U. (a) Band structures of unit cells with different radii. Other parameters are the same as those in Fig. 4 and the radius is in millimeters. (b)–(d) Band diagram for supercells with fixed $N_x = 4$ and different r_2.

[1] Z. Wang, Y. Sun, X.-Q. Chen, C. Franchini, G. Xu, H. Weng, X. Dai, and Z. Fang, Dirac semimetal and topological phase transitions in A_3Bi (A = Na, K, Rb), Phys. Rev. B **85**, 195320 (2012).

[2] Z. Liu, B. Zhou, Y. Zhang, Z. Wang, H. Weng, D. Prabhakaran, S.-K. Mo, Z. Shen, Z. Fang, and X. Dai, Discovery of a three-dimensional topological Dirac semimetal, Na_3Bi, Science **343**, 864 (2014).

[3] J. Xiong, S. K. Kushwaha, T. Liang, J. W. Krizan, M. Hirschberger, W. Wang, R. J. Cava, and N. P. Ong, Evidence for the chiral anomaly in the Dirac semimetal Na_3Bi, Science **350**, 413 (2015).

[4] A. Burkov, M. Hook, and L. Balents, Topological nodal semimetals, Phys. Rev. B **84**, 235126 (2011).

[5] C. Fang, Y. Chen, H.-Y. Kee, and L. Fu, Topological nodal line semimetals with and without spin-orbital coupling, Phys. Rev. B **92**, 081201(R) (2015).

[6] N. Ong and S. Liang, Experimental signatures of the chiral anomaly in Dirac–Weyl semimetals, Nat. Rev. Phys. **3**, 394 (2021).

[7] N. Schröter, D. Pei, M. G. Vergniory, Y. Sun, K. Manna, F. De Juan, J. Krieger, V. Süss, M. Schmidt, and P. Dudin, Chiral topological semimetal with multifold band crossings and long Fermi arcs, Nat. Phys. **15**, 759 (2019).

[8] X. Wan, A. M. Turner, A. Vishwanath, and S. Y. Savrasov, Topological semimetal and Fermi-arc surface states in the electronic structure of pyrochlore iridates, Phys. Rev. B **83**, 205101 (2011).

[9] A. Burkov and L. Balents, Weyl Semimetal in a Topological Insulator Multilayer, Phys. Rev. Lett. **107**, 127205 (2011).

[10] X. Huang, L. Zhao, Y. Long, P. Wang, D. Chen, Z. Yang, H. Liang, M. Xue, H. Weng, and Z. Fang, Observation of the Chiral-Anomaly-Induced Negative Magnetoresistance in 3D Weyl Semimetal TaAs, Phys. Rev. X **5**, 031023 (2015).

[11] M. Xiao, W.-J. Chen, W.-Y. He, and C. T. Chan, Synthetic gauge flux and Weyl points in acoustic systems, Nat. Phys. **11**, 920 (2015).

[12] S.-Y. Xu, I. Belopolski, N. Alidoust, M. Neupane, G. Bian, C. Zhang, R. Sankar, G. Chang, Z. Yuan, and C.-C. Lee, Discovery of a Weyl fermion semimetal and topological Fermi arcs, Science **349**, 613 (2015).

[13] B. Lv, H. Weng, B. Fu, X. P. Wang, H. Miao, J. Ma, P. Richard, X. Huang, L. Zhao, and G. Chen, Experimental Discovery of Weyl Semimetal TaAs, Phys. Rev. X **5**, 031013 (2015).

[14] W.-J. Chen, M. Xiao, and C. T. Chan, Photonic crystals possessing multiple Weyl points and the experimental observation of robust surface states, Nat. Commun. **7**, 13038 (2016).

[15] H. He, C. Qiu, L. Ye, X. Cai, X. Fan, M. Ke, F. Zhang, and Z. Liu, Topological negative refraction of surface acoustic waves in a Weyl phononic crystal, Nature (London) **560**, 61 (2018).

[16] Q. Lin, M. Xiao, L. Yuan, and S. Fan, Photonic Weyl point in a two-dimensional resonator lattice with a synthetic frequency dimension, Nat. Commun. **7**, 13731 (2016).

[17] B. Yang, Q. Guo, B. Tremain, R. Liu, L. E. Barr, Q. Yan, W. Gao, H. Liu, Y. Xiang, and J. Chen, Ideal Weyl points and helicoid surface states in artificial photonic crystal structures, Science **359**, 1013 (2018).

[18] H. B. Nielsen and M. Ninomiya, The Adler-Bell-Jackiw anomaly and Weyl fermions in a crystal, Phys. Lett. B **130**, 389 (1983).

[19] H.-J. Kim, K.-S. Kim, J.-F. Wang, M. Sasaki, N. Satoh, A. Ohnishi, M. Kitaura, M. Yang, and L. Li, Dirac versus Weyl Fermions in Topological Insulators: Adler-Bell-Jackiw Anomaly in Transport Phenomena, Phys. Rev. Lett. **111**, 246603 (2013).

[20] Q. Li, D. E. Kharzeev, C. Zhang, Y. Huang, I. Pletikosić, A. Fedorov, R. Zhong, J. Schneeloch, G. Gu, and T. Valla, Chiral magnetic effect in $ZrTe_5$, Nat. Phys. **12**, 550 (2016).

[21] R. Ilan, A. G. Grushin, and D. I. Pikulin, Pseudo-electromagnetic fields in 3D topological semimetals, Nat. Rev. Phys. **2**, 29 (2020).

[22] D. Pikulin, A. Chen, and M. Franz, Chiral Anomaly from Strain-Induced Gauge Fields in Dirac and Weyl Semimetals, Phys. Rev. X **6**, 041021 (2016).

[23] Y. Zhang, Y.-W. Tan, H. L. Stormer, and P. Kim, Experimental observation of the quantum Hall effect and Berry's phase in graphene, Nature (London) **438**, 201 (2005).

[24] K. S. Novoselov, A. K. Geim, S. V. Morozov, D. Jiang, M. I. Katsnelson, I. Grigorieva, S. Dubonos, and A. Firsov, Two-dimensional gas of massless Dirac fermions in graphene, Nature (London) **438**, 197 (2005).

[25] G. Li, A. Luican-Mayer, D. Abanin, L. Levitov, and E. Y. Andrei, Evolution of Landau levels into edge states in graphene, Nat. Commun. **4**, 1744 (2013).

[26] L. Lu, J. D. Joannopoulos, and M. Soljačić, Topological photonics, Nat. Photonics **8**, 821 (2014).

[27] G. Ma, M. Xiao, and C. T. Chan, Topological phases in acoustic and mechanical systems, Nat. Rev. Phys. **1**, 281 (2019).

[28] T. Ozawa, H. M. Price, A. Amo, N. Goldman, M. Hafezi, L. Lu, M. C. Rechtsman, D. Schuster, J. Simon, and O. Zilberberg, Topological photonics, Rev. Mod. Phys. **91**, 015006 (2019).

[29] K. Fang, Z. Yu, and S. Fan, Realizing effective magnetic field for photons by controlling the phase of dynamic modulation, Nat. Photonics **6**, 782 (2012).

[30] X. Wen, C. Qiu, Y. Qi, L. Ye, M. Ke, F. Zhang, and Z. Liu, Acoustic Landau quantization and quantum-Hall-like edge states, Nat. Phys. **15**, 352 (2019).

[31] M. C. Rechtsman, J. M. Zeuner, A. Tünnermann, S. Nolte, M. Segev, and A. Szameit, Strain-induced pseudomagnetic field and photonic Landau levels in dielectric structures, Nat. Photonics **7**, 153 (2013).

[32] Z. Yang, F. Gao, Y. Yang, and B. Zhang, Strain-induced Gauge Field and Landau Levels in Acoustic Structures, Phys. Rev. Lett. **118**, 194301 (2017).

[33] H. Jia, R. Zhang, W. Gao, Q. Guo, B. Yang, J. Hu, Y. Bi, Y. Xiang, C. Liu, and S. Zhang, Observation of chiral zero mode in inhomogeneous three-dimensional Weyl metamaterials, Science **363**, 148 (2019).

[34] S. Kiriushechkina, A. Vakulenko, D. Smirnova, S. Guddala, F. Komissarenko, M. Allen, J. Allen, and A. B. Khanikaev, Photonic dirac waveguides, arXiv:2211.00701.

[35] V. Peri, M. Serra-Garcia, R. Ilan, and S. D. Huber, Axial-field-induced chiral channels in an acoustic Weyl system, Nat. Phys. **15**, 357 (2019).

[36] H. Jia, M. Wang, S. Ma, R.-Y. Zhang, J. Hu, and C. T. Chan, Experimental realization of chiral Landau levels in two-dimensional Dirac cone systems with inhomogeneous effective mass, arXiv:2209.10745.

[37] M. Wang, Q. Ma, S. Liu, R.-Y. Zhang, L. Zhang, M. Ke, Z. Liu, and C. T. Chan, Observation of boundary induced

chiral anomaly bulk states and their transport properties, Nat. Commun. **13**, 5916 (2022).

[38] J. Lu, C. Qiu, L. Ye, X. Fan, M. Ke, F. Zhang, and Z. Liu, Observation of topological valley transport of sound in sonic crystals, Nat. Phys. **13**, 369 (2017).

[39] X. Wu, Y. Meng, J. Tian, Y. Huang, H. Xiang, D. Han, and W. Wen, Direct observation of valley-polarized topological edge states in designer surface plasmon crystals, Nat. Commun. **8**, 1304 (2017).

[40] Z.-K. Shao, H.-Z. Chen, S. Wang, X.-R. Mao, Z.-Q. Yang, S.-L. Wang, X.-X. Wang, X. Hu, and R.-M. Ma, A high-performance topological bulk laser based on band-inversion-induced reflection, Nat. Nanotechnol. **15**, 67 (2020).

[41] W. Wang, X. Wang, and G. Ma, Non-Hermitian morphing of topological modes, Nature (London) **608**, 50 (2022).

[42] G. Harari, M. A. Bandres, Y. Lumer, M. C. Rechtsman, Y. D. Chong, M. Khajavikhan, D. N. Christodoulides, and M. Segev, Topological insulator laser: Theory, Science **359**, eaar4003 (2018).

[43] M. A. Bandres, S. Wittek, G. Harari, M. Parto, J. Ren, M. Segev, D. N. Christodoulides, and M. Khajavikhan, Topological insulator laser: Experiments, Science **359**, eaar4005 (2018).

[44] J. Chen and Z.-Y. Li, Prediction and Observation of Robust One-Way Bulk States in a Gyromagnetic Photonic Crystal, Phys. Rev. Lett. **128**, 257401 (2022).

[45] M. Wang, R.-Y. Zhang, L. Zhang, D. Wang, Q. Guo, Z.-Q. Zhang, and C. T. Chan, Topological One-Way Large-Area Waveguide States in Magnetic Photonic Crystals, Phys. Rev. Lett. **126**, 067401 (2021).

[46] K. Nakada, M. Fujita, G. Dresselhaus, and M. S. Dresselhaus, Edge state in graphene ribbons: Nanometer size effect and edge shape dependence, Phys. Rev. B **54**, 17954 (1996).

[47] W. Yao, S. A. Yang, and Q. Niu, Edge States in Graphene: From Gapped Flat-Band to Gapless Chiral Modes, Phys. Rev. Lett. **102**, 096801 (2009).

[48] M. P. Makwana and G. Chaplain, Tunable three-way topological energy-splitter, Sci. Rep. **9**, 18939 (2019).

[49] T. Baba, Slow light in photonic crystals, Nat. Photonics **2**, 465 (2008).